Cement and Concrete Composites 134 (2022) 104790

Contents lists available at ScienceDirect

Cement and Concrete Composites

journal homepage: www.elsevier.com/locate/cemconcomp

Material processing, microstructure, and composite properties of low carbon Engineered Cementitious Composites (ECC)

Mengjun Hou, Duo Zhang, Victor C. Li *

Department of Civil and Environmental Engineering, University of Michigan, Ann Arbor, MI, USA

ARTICLE INFO

Keywords:
Engineered cementitious composites (ECC)
Limestone calcined clay cement (LC3)
Polypropylene (PP) fiber
Rheological properties
Microstructure
Mechanical properties

ABSTRACT

Traditional PVA fiber-reinforced Engineered Cementitious Composites (ECC) show high tensile ductility and superior durability with tight crack width, but the high cost and embodied carbon can hinder its wider application in infrastructures. The objective of this study is to develop a better understanding of the fresh and hardened properties of an ECC that employs a lower embodied-carbon binder, Limestone Calcined Clay Cement (LC3), and lower-cost PP fiber that is widely available. Specifically, the interrelations between material processing, microstructure, and composite properties were studied experimentally. The results showed that ECC with high tensile ductility up to 9% tensile strain and tight crack width with 50 μm at 2% tensile strain can be achieved. It was found that a matrix paste with higher viscosity generally enhanced fiber dispersion uniformity and robustness in tensile strain-hardening. The paste viscosity is increased when OPC is replaced by LC3 and can be tuned with superplasticizer content. Larger maximum flaw size leads to lower first crack strength, beneficial for microcrack initiation and multiple cracking. This study generates fundamental knowledge linking processing-microstructure-performance of PP-LC3-ECC. This class of low embodied carbon ECC with tight crack width is expected to contribute to reducing the carbon footprint of the built environment.

1. Introduction

Engineered Cementitious Composite (ECC) is a high-performance cementitious material designed based on micromechanics to achieve extreme tensile ductility. ECC consists of typical concrete raw materials and randomly oriented short fibers at a low volume fraction (typically less than 2 vol%) minus the coarse aggregates. Based on micromechanics models, fiber, matrix, and fiber/matrix interfacial properties are tailored to satisfy the pseudo-strain-hardening conditions [1]. ECC has a tensile ductility of at least 2%, 200 times that of conventional concrete. In addition, ECC exhibits multiple cracking behaviors during the strain-hardening stage. The crack width of ECC stabilizes at a constant range autogenously (typically 50–100 μm for PVA-ECC) even when deformed beyond the elastic range. The unique feature of multiple microcracks effectively improves the durability of infrastructure. Both laboratory and natural exposure studies proved ECC's excellent ductility, tight cracks, and the improvement in the durability of infrastructures [2–5]. However, compared to conventional concrete, early versions of ECC have high embodied energy and carbon since a large amount of Portland cement is used in the ECC mixture due to the elimination of coarse aggregate. The energy and carbon intensities of ECC are further enlarged by the reinforcing synthetic fibers even at a small fiber dosage [6].

Ordinary Portland cement production incurs high CO_2 emissions [7], accounting for 5–8% of global anthropogenic CO_2 emissions [8–11]. One well-known strategy to enhance the sustainability of concrete is to reduce cement content by incorporating Supplementary Cementitious Materials (SCM). Fly ash, slag, and limestone have been successfully used to reduce the clinker factor and account for over 80% of SCMs in the past decades [12]. In recent years, clay has been combined with limestone and OPC to produce calcined clay limestone cement (LC3), which has a similar mechanical performance to ordinary cement [12–14]. It was reported that 15% of the cost, 20% of energy, and 30% of CO_2 emissions were reduced by replacing 50% of OPC with limestone and metakaolin clay [12,15–17].

LC3 binder has been used in ECC composite recently. Zhang et al. [18] applied LC3 binder to PVA ECC, and found that LC3-based ECC showed more rapid early strength development, while the tensile strain capacity of LC3-based ECC achieved over 6% with an average residual crack width less than 50 μm. Additionally, the composite pore structure

* Corresponding author.
E-mail address: vcli@umich.edu (V.C. Li).

https://doi.org/10.1016/j.cemconcomp.2022.104790
Received 12 March 2022; Received in revised form 6 September 2022; Accepted 26 September 2022
Available online 29 September 2022

exhibited a decreasing volume fraction of large pores and voids (>100 nm) after substituting LC3 for OPC. Yu et al. [19] used an ultrahigh-volume limestone-clay blend and found that PVA-ECC can achieve sufficient early strength and medium long-term strength. Zhu et al. [20,21] developed sprayable ECC with LC3 binder and PP fiber. This composite possesses a tensile strain capacity greater than 6% and an intrinsically tight crack width below 82 μm when loaded to 1% tensile strain. Wang et al. [22] found that the formation of highly polymerized C-A-S-H gel and abundant ettringite improved the flexural strength of LC3. While these background studies establish the feasibility of using LC3 as a greener binder in ECC, the robustness of tensile strain capacity of ECC depends on multiple factors, including mixture composition design, material processing and microstructure, and knowledge of their interactions with composite properties remains limited.

To further reduce the embodied energy and carbon of ECC, the fiber type also plays an important role. Compare to PVA fiber which is widely used in the current ECCs, polypropylene (PP) fiber is less-costly, more environmentally friendly, and widely available [23–26]. However, the mechanical properties of ECC are deteriorated by undesired fiber dispersion [25,27–35]. Due to the large fiber aspect ratio (fiber length/diameter), fibers tend to bend and cluster in the matrix. Among the different types of fibers used in ECC, PP fiber has the smallest diameter of 12 μm and the highest aspect ratio (1000 in the present study), which further increases the difficulty of PP fiber dispersion in the ECC matrix. Rheology control is important for uniform fiber distribution to obtain desired mechanical properties. This can be achieved in two ways by changing mixture design (e.g. ingredients and w/b ratio) [34], and chemical admixtures (e.g. superplasticizer (SP) and viscosity modifying admixtures (VMA)) [35,36]. Besides, the mixing and casting skills are also critical to good fiber dispersion and ECC production quality [25,37]. On the other hand, the tensile properties of ECC are known to be also sensitive to the flaw size distribution, which is related to the matrix flowability and mixing processing [37,38]. Although both fiber dispersion and flaw size distribution are dependent on the matrix fresh properties and mixing processing, the majority of existing research is only focused on the effect of one of these processing parameters, and the interrelation between these parameters and mechanical properties is barely studied.

Based on the above discussion, the relatively newer class of ECC employing an LC3 binder and reinforced with PP fiber (LC3-PP-ECC) hold promise as a greener version of ECC. Specifically, LC3-PP-ECC shows a reduction of 41–45%, 22–26%, and 33–35% in cost, embodied energy, and carbon emission, respectively [6], when compared with the widely studied OPC-based ECC reinforced with PVA fiber. The objective of this study is to develop a better understanding of the interrelationships between composition, processing parameters, microstructure, and composite properties of this newer class of ECC. The research framework is illustrated in Fig. 1. Specifically, the influence of matrix fresh properties, fiber dispersion, and flaw size distribution on mechanical performance was investigated. A preliminary study indicates a higher viscosity of LC3 paste compared to that of OPC paste. A decision was made to control the paste rheology by adjusting the amount of superplasticizer content, without the use of the viscosity modifying agent as previously employed [32]. The rheological properties of ECC were determined using a rheometer. The tensile, compressive, and single-crack tests were conducted. After the tension test, each dogbone specimen was sectioned within the gauge region, and the maximum flaw size on each cross-section was measured. The fiber dispersion was determined via fluorescence microscopy and quantified as fiber dispersion coefficients. Finally, the influence of matrix fresh properties, fiber dispersion, and flaw size distribution on mechanical performance was analyzed. The research findings provide a foundation for a deeper understanding of the influence of LC3 and SP on fiber dispersion uniformity, flaw size distribution, and tensile properties of LC3-PP-ECC.

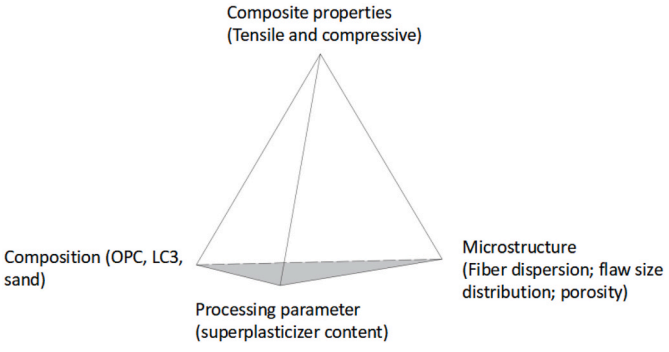

Fig. 1. Research framework: The composite microstructure is strongly influenced by mix composition and process control, and in turn governs the composite tensile and compressive properties of LC3-PP-ECC.

2. Experimental studies

2.1. Mix design and materials

The raw materials in the experiment include Type I ordinary Portland cement (OPC), metakaolin (MK), limestone (LM), ASTM Class C fly ash (FA), F75 silica sand, and tap water. In the LC3 binder, the ratio of OPC: MK: LM was 0.5:0.25:0.25. The superplasticizer (SP) from BASF (MasterGlenium 7920) was adopted as a high-range water reducer. The chemical compositions and particle size distribution of the materials used in this study are shown in Table 1 and Fig. 2, respectively. Polypropylene (PP) fiber with properties shown in Table 2 was used in all mixtures.

Six batches of ECC specimens were prepared according to the mix proportions in Table 3. M1 mix composition represents conventional OPC-based ECC as a control group. M2 and M3 mix composition represent the LC3-based ECC. Fine sand is usually included in ECC. To investigate the influence of sand on rheological and hardened properties, the M2 mix does not include sand. SP dosage was adjusted for M1, M2, and M3 (M3-S10) to keep similar fresh composite flowability and aimed at a minimum of 150 mm for ease of casting [35]. For M3, four SP dosages (8, 10, 12, and 16 kg/m^3) were used to investigate the effect of superplasticizer as a process admixture on the fresh properties, fiber dispersion, flaw size distribution, and mechanical properties of ECC.

2.2. Mixing procedure and fresh property characterization

According to the literature [25,35], good PP fiber dispersion in cementitious materials requires proper mixer type, mixing force/speed, mixing time, and optimal viscosity of the matrix. In this study, an 18-liter Hobart mixer was adopted. The dry ingredients (without fibers) were mixed for 5 min at slow speed (54 rpm) to ensure sufficient blending, after which, the water premixed with superplasticizer was added into the mixing bowl slowly and then mixed for another 5 min at medium speed (100 rpm) to achieve the desired matrix flowability.

Before the fiber addition, the rheological properties of the fresh matrix were measured using an ICAR rheometer. After the fresh matrix was filled into the rheometer container, the blade vane with a diameter of 127 mm and a height of 127 mm was carefully inserted into the matrix before the flow curve test. As shown in Fig. 3(a), the flow curve test was initiated by a pre-shear period (60 s) with the maximum test speed (0.5 rps) to minimize the effects of thixotropy and provide a consistent shear history. And then the vane was rotated at decreasing speed with decrements of 0.05 rps from 0.5 rps to 0.05 rps. With a 5 s period for each speed, corresponding torque was measured and recorded. The initial corresponding shear rate is around 97 s^{-1} at the middle of the vane blade, which is comparable to the test protocols of other types of rheometer [31,36,39–42]. No measurements were made during the

Table 1
Chemical composition of the binder materials (%).

	CaO	SiO_2	Fe_2O_3	Al_2O_3	SO_3	Na_2O	K_2O	MgO	TiO_2	LOI
OPC	61.74	20.48	3.07	4.46	2.56	0.09	0.43	3.20	0.22	2.10
MK	0.04	51.41	0.33	43.04	0.05	0.20	0.10	0.00	1.56	1.43
LM	55.00	0.80	0.30	0.30	0.00	0.00	0.00	1.80	0.00	41.80
FA	17.41	39.35	11.00	19.76	1.91	1.13	1.07	3.70	0.00	1.30

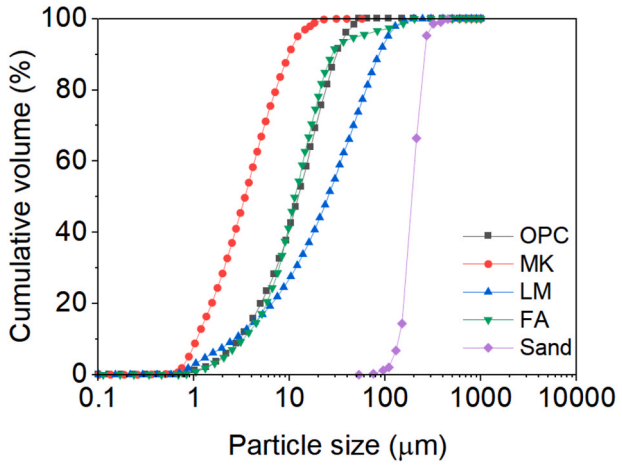

Fig. 2. Particle size distribution of ingredient materials used in this study.

Table 2
Properties of PP fiber.

Diameter/ μm	Length/ mm	Strength/ MPa	Elastic modulus/ GPa	Elongation/ %	Density/ (g/cm^3)
12	12	910	9	22	0.91

Table 3
Mix proportion of ECC (kg/m^3).

Mixture ID	OPC	MK	LS	FA	Sand	Water	SP	PP[a]
M1	716	0	0	716	358	358	7	2%
M2	404	202	202	808	0	404	9	2%
M3-S8	350	175	175	700	350	350	8	2%
M3-S10	350	175	175	700	350	350	10	2%
M3-S12	350	175	175	700	350	350	12	2%
M3-S16	350	175	175	700	350	350	16	2%

[a] Volume fraction.

pre-shear period, and the torque and rotational speed readings for each speed are plotted as shown in Fig. 3(b) for further rheological parameters computation. Since the linear relation fitted well with the observed data, the Bingham model as shown in Eq. (1) is suitable for the rheological analysis in this study. The yield stress and plastic viscosity were computed by the embedded software in the rheometer, enabling their instant read-out at the end of each test.

$$\tau = \tau_0 + \mu\dot{\gamma} \tag{1}$$

where τ_0 is the yield stress, μ is the plastic viscosity, and $\dot{\gamma}$ is the shear rate.

After measuring the rheological parameters, the matrix was poured into a clean mixer container. Potential material loss during transfers was accounted for. Then the matrix was mixed for an additional 2 min at medium speed. After fiber addition, the fresh composite was mixed for 2 min at medium speed and another 5 min at high speed (183 rpm) for a thorough fiber dispersion. Before casting into the molds, the flowability of fresh ECC was measured by a flow table test following ASTM C1437 [43].

2.3. Specimen preparation and testing

After the completion of the fresh properties test, the fresh mixtures were cast into 50 × 50 × 50 mm^3 cubes and dogbone-shaped molds on a vibration table. After pouring the fresh composites into the molds, the vibration last for 30 s to help the fresh ECC settle uniformly into the mold. The dogbone-shaped specimen geometry as per JSCE [44] is shown in Fig. 4(a). The specimens were demolded after 24 h and cured in the air for 28 days before testing. These specimens were used for experimental determination of compressive and tensile properties, as well as for the determination of fiber dispersion uniformity, maximum defect size distribution, and porosity. Cube specimens were tested in compression following ASTM C109 [45]. The uniaxial tension test was conducted with the dogbone-shaped specimens on an Instron servo-hydraulic system under displacement control at a rate of 0.5 mm/min. Two external linear variable displacement transducers (LVDT) were attached to the specimen and the gage length is 80 mm. Then the tensile stress-strain relationship was determined to analyze the tensile behavior of specimens. Single crack dogbone specimens (Fig. 4(b)) were used to determine the fiber bridging stress-crack opening (σ−δ) relationship of mixtures, following the same procedure for uniaxial tension test. The opening of the single crack was measured by a pair of LVDT.

In addition, the matrix beam specimens (38 × 76 × 305 mm^3) were prepared to determine the fracture toughness of the matrix. Three matrix beam specimens for each mixture were pre-notched with a diamond cutting saw prior to the three-point bending test following ASTM E399 [46]. The relative notch depth ratio was kept to be 0.3. As shown in Fig. 5, the specimen was supported over a load span (S = 254 mm) and the bending test was performed under the displacement control rate of 0.02 mm/min. The linear elastic fracture mechanics (LEFM) method [47] was used to determine fracture toughness due to the small fracture process zone size in the matrix without coarse aggregate. The fracture toughness K_m can be calculated by the following equations.

$$K_m = \frac{PS}{BW^{1.5}} \bullet f(\alpha) \tag{2}$$

$$f(\alpha) = 3\sqrt{\alpha} \bullet \frac{1.99 - \alpha(1-\alpha)(2.15 - 3.93\alpha + 2.7\alpha^2)}{2(1+2\alpha)(1-\alpha)^{1.5}} \tag{3}$$

where P is the maximum load; S is the span of the beam; B is the width of the beam; W is the specimen height; $\alpha = a/W$ is the relative notch depth ratio; a is the notch depth.

To examine fiber dispersion uniformity and the distribution of maximum flaw size from one plane to another, the uniaxially tested dogbone specimens were sectioned using a diamond blade saw perpendicular to the loading direction. Specifically, the LVDT gauge length region was cut into 8 bulk sections each around 10 mm in thickness. Due to the thickness of the saw blade, 2–3 mm thickness for each cutting section was lost, thus differentiating the shared surface of adjacent bulks. Therefore, it was reasonable to count both surfaces for each sectioned bulk, totaling 16 surfaces for each specimen and 64 cross-sections for each mixture. The cross-section where the specimen reached final failure was included intentionally. All cross-sections were ground to a smooth surface before measurement.

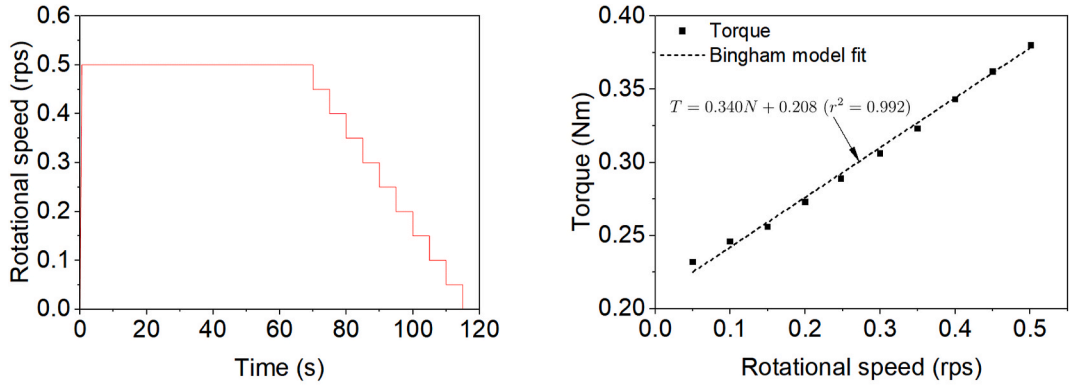

(a) Rheology testing protocol (b) A typical torque-rotational speed relation

Fig. 3. Rheology testing protocol and results (a) Rheology testing protocol, (b) A typical torque-rotational speed relation.

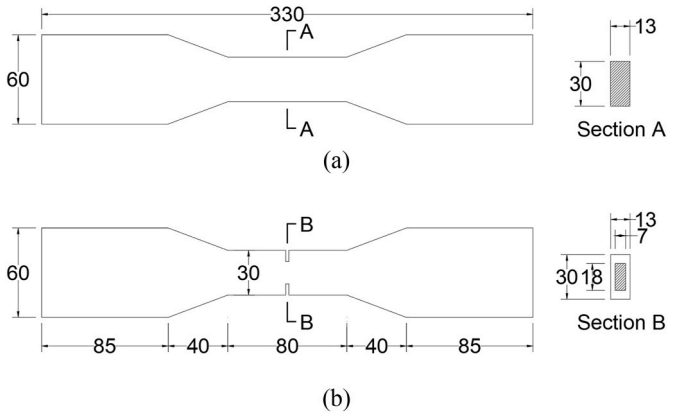

Fig. 4. Dimensions of dogbone-shaped specimen for (a) uniaxial tension and (b) single-crack test (unit: mm).

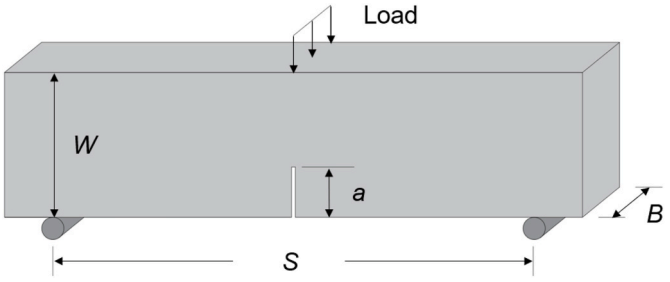

Fig. 5. Three-point bending test set-up.

Despite the multiple voids on each cross-section, the largest ones are assumed to initiate the micro-cracks based on the ECC design theory. The maximum flaw size on each cross-section was measured to investigate the effect of fresh properties on the flaw size distribution and further on the mechanical properties of ECC. Since the voids are at millimeter size, a vernier caliper was used to measure their size and the value was accurate at 0.1 mm. Given that most voids are irregular in the shape of ellipses, the flaw size was considered as the average of the major and minor axis for simplicity. For each mixture, a total of 64 data points were classified with a 0.5 mm size gap, and the data analysis is discussed in Section 3.2.2.

To evaluate fiber dispersion, fluorescence microscopy (Fig. 6(a)) was used to examine three randomly chosen cross-sections in addition to the failure cross-section. PP fibers fluoresce when excited by ultraviolet light with a wavelength of 330–380 nm. The fluorescence image reveals fibers as bright spots against the dark background of the cementitious matrix [48–50]. This image was captured by a digital camera with a field of view of 4.2 × 3.2 mm^2 in 1392 × 1040 pixels. To eliminate the specimen edge effects, the observation area started from 1 mm inside the cross-section. For each cross-section, 15 images were captured from the grid region as shown in Fig. 6(b). The original images were processed with noise filtering, binary, and number count via ImageJ software. As PP fiber has a relatively small diameter, the larger bright dots that might indicate inclined or bundled fibers were considered as one fiber. Fiber dispersion was quantified by fiber dispersion coefficient α according to Eq. (4), which represents the deviation of the number of fibers from the average fiber numbers in the unit area.

$$\alpha = \exp\left[-\sqrt{\frac{\sum (x_i - \bar{x})^2}{n}} \Big/ \bar{x}\right] \tag{4}$$

where x_i is the number of fibers in the ith unit area; $\bar{x}$ is the average number of fibers for a unit area; n is the number of unit areas. α ranges between 0 and 1, with larger values representing higher fiber uniformity.

The porosity P of cube specimens was computed using Eq. (5) based on their bulk density ρ_0 and particle density ρ. The bulk density was experimentally determined, while the particle density was computed based on the density of the individual components in the composite, assuming perfect packing.

$$P = \left(1 - \frac{\rho_0}{\rho}\right) \times 100\% \tag{5}$$

3. Results and discussion

3.1. Fresh properties

The fresh properties of each mixture are shown in Table 4. When OPC was replaced by the LC3 binder, more superplasticizer was needed to maintain the proper flowability for the fresh mixtures with fibers. Specifically, compared to the OPC-based ECC mixture, M1, which required 7 kg/m^3 of SP to keep the proper flowability, the LC3 binder mixture, M2 and M3-S10, required 9 kg/m^3 and 10 kg/m^3 of SP to maintain a similar flowability. Further, when OPC was replaced by the LC3 binder, the paste viscosity increased from 2.39 Pa■s (M1) to 4.26 Pa■s (M3-S10) even with more superplasticizers used. This is consistent with the literature [51,52]. The use of calcined clay increased the water demand due to its high fineness and narrow particle size distribution [53]. Besides, polycarboxylate ether (PCE) superplasticizers are sensitive to clays. The Ca^{2+} ions released by cement dissolution tend to adsorb onto

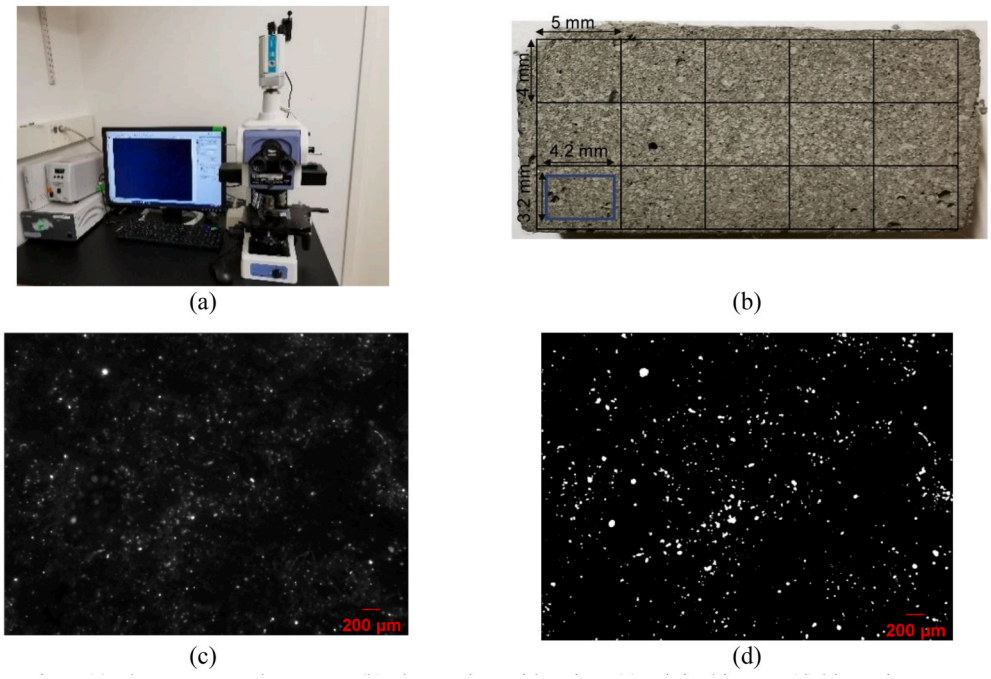

Fig. 6. (a) Fluorescence microscope; (b) observation grid region; (c) original image; (d) binary image.

Table 4
Fresh properties of mixtures.

Mixture ID		M1	M2	M3-S8	M3-S10	M3-S12	M3-S16
Superplasticizer (SP) (kg/m^3)		7	9	8	10	12	16
Matrix	Yield stress (Pa)	21.26	46.21	69.82	23.05	15.23	8.72
	Viscosity (Pa■s)	2.39	4.46	4.48	4.26	1.29	0.54
Composite	Spread diameter (mm)	168 ± 5	169 ± 4	154 ± 6	167 ± 4	168 ± 9[a]	169 ± 3[a]

[a] Water bleeding observed.

the calcined clay surface which is initially negatively charged, and this layer of adsorbed Ca^{2+} ions facilitates the adsorption of anionic PCE superplasticizers [54,55]. M2 without silica sand showed higher yield stress and viscosity than the mixture with silica sand (M3-S10) due to the higher volume of binder in the unit matrix volume. For the same mixture composition, increasing SP content lowered the yield stress and viscosity of the matrix. Fig. 7 indicates the decreasing linear relationship between SP content and rheological parameters, and even a stronger coefficient of determination with viscosity. This trend is consistent with that reported in the literature [56]. The adsorption of the backbone of PCEs to the binder surface results in electrostatic repulsion to break the flocculated structure and release free water inside. Meanwhile, the side chains of PCEs can stretch out as the steric hindrance to help disperse the cement particles as well [57]. Increasing SP content lowered the yield stress and viscosity but did not increase the flowability of fresh fiber-reinforced composite significantly, and such paste tends to bleed (e.g., Fig. 8, when SP content reached beyond 12 kg/m^3).

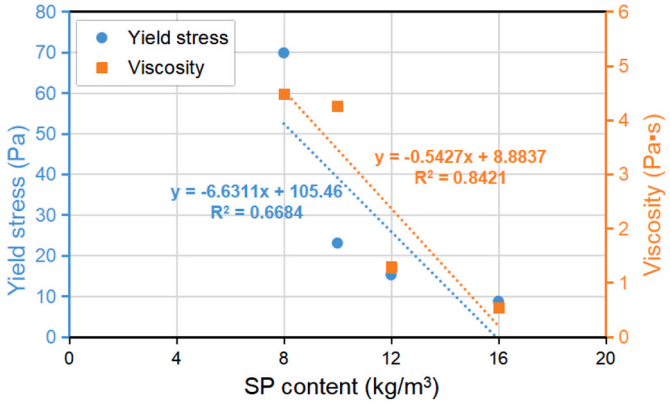

Fig. 7. Increasing SP content diminishes the rheological parameters for Mixture M3.

3.2. Microstructure analyses

3.2.1. Fiber dispersion

The relationship between matrix viscosity and fiber dispersion coefficient is presented in Fig. 9. The fiber dispersion coefficients for all mixtures were above 0.75, indicating a good fiber dispersion compared to those previously reported for PP fibers [35] at a lower matrix viscosity. Fiber dispersion uniformity is dependent on multiple factors. Matrix viscosity is proved important for fiber distribution and there is an optimal value and recommended range for good fiber dispersion with different fiber types [28,35]. However, the optimal value is a relative definition since other factors, e.g., mixing procedure, are also critical for good fiber dispersion. A short mixing time or small mixing force cannot break up fiber bundles thoroughly even at a proper matrix viscosity. In this study, an optimized mixing procedure with sufficient mixing time and force/speed was adopted to ensure fiber distribution, and therefore good fiber distribution can be obtained at a relatively low matrix viscosity.

In general, fiber dispersion is enhanced by increased viscosity, which in turn is influenced by the amount of superplasticizer and the matrix composition. There is a linearly increasing relationship between viscosity and fiber dispersion coefficients as shown in Fig. 9. Compared to M3-S10, the absence of silica sand in M2 reveals a higher viscosity and better fiber distribution. Increasing SP dosage from 8 kg/m^3 to 16 kg/m^3 leads to decreasing matrix viscosity (4.48 → 0.54 Pa■s) and a

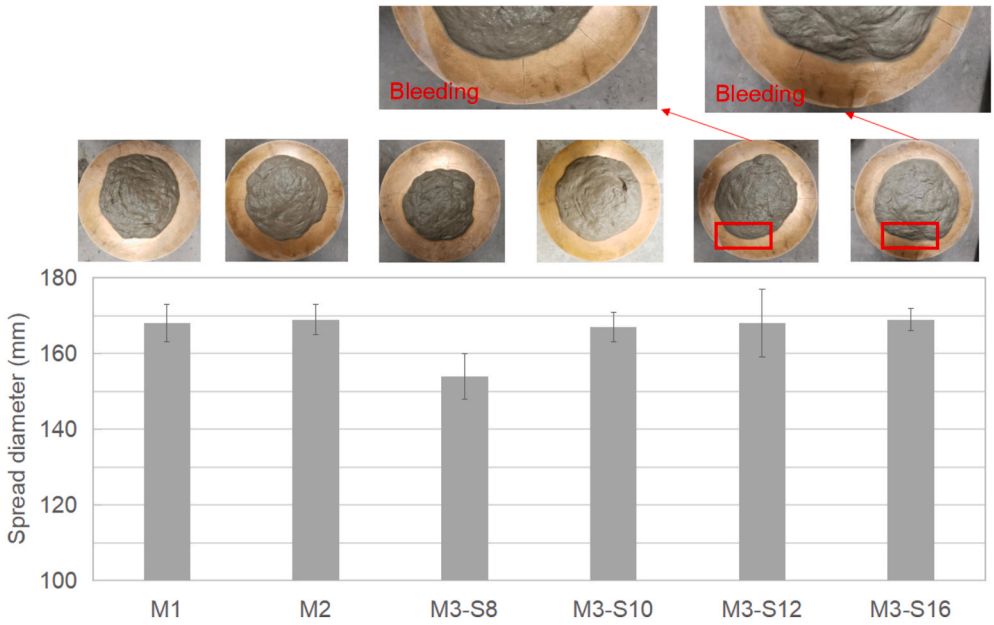

Fig. 8. Flow table test results show similar flowability quantified by spread diameter for M1, M2, and M3-S10. M3-S8 with lower SP content shows reduced flowability, while M3-S12 and M3-S16 with higher SP content show a tendency to bleed.

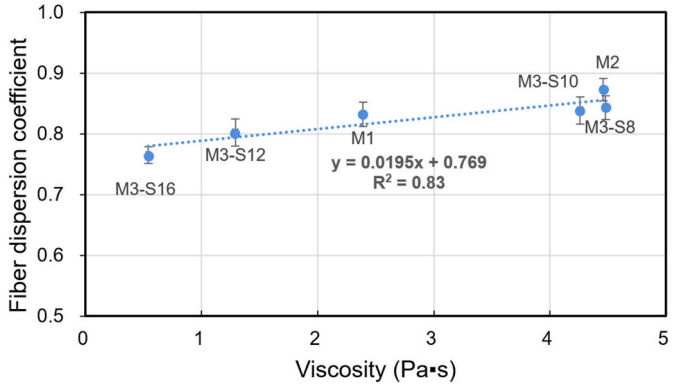

Fig. 9. Relationship between matrix plastic viscosity and fiber dispersion coefficients.

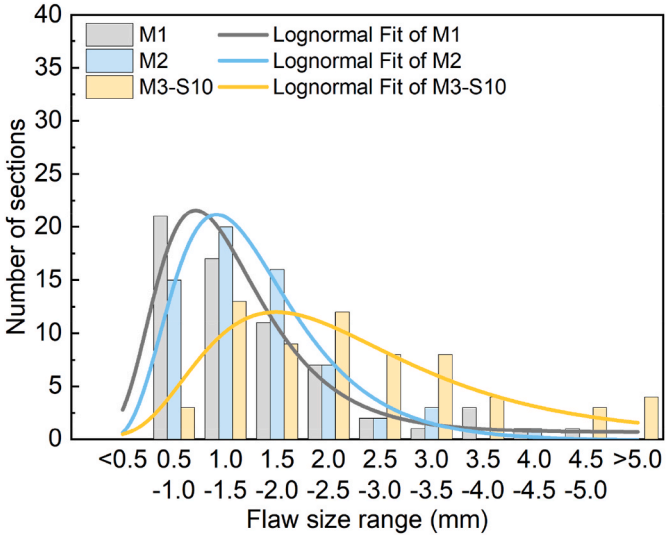

Fig. 10. Maximum flaw size distribution for 64 sections (16 × 4) of M1, M2, and M3-S10.

corresponding decrease in fiber dispersion coefficient from 0.843 to 0.765, as revealed in the Mixture series M3-S8, M3-S10, M3-S12, and M3-S16. As discussed above, slight bleeding and relatively small changes in spread diameter were observed at high SP content, nevertheless, the fiber distribution can be ensured by an optimized mixing procedure.

3.2.2. *Flaw size distribution*

The maximum flaw size for each cross-section of the M1, M2, and M3-S10 was recorded, and the data is presented as a histogram with lognormal fit curves in Fig. 10. The fitted curves indicate that most of the large size flaws fall in the range of 0.5–2.5 mm for M1 and M2, and in the range of 1.0–3.5 mm for M3-S10. M3-S10 has the biggest max flaw size beyond 5 mm, followed by 4.5–5.0 mm for M1 and 4.0–4.5 mm for M2.

It was observed that the section with the biggest max flaw size for each specimen was not always the failure section. Instead, the low fiber-bridging capacity at a particular section determines the final failure plane. As shown in Fig. 11, the max flaw size was in Section 2L but the failure crack in Bulk 4 connects Section 4L and Section 4R. The air voids were so close that the net cross-section area and fiber content were reduced, which led to the weakest fiber bridging [28,58]. This should be expected for a strain-hardening fiber composite since the composite failure at ultimate tensile strength is governed by the specimen section with the lowest fiber-bridging capacity. However, the first crack strength is related to the maximum flaw size and matrix fracture toughness according to fracture mechanics, $\sigma = K_m/(Y\sqrt{\pi a})$, where K_m is matrix fracture toughness, a is the maximum flaw size, Y is a dimensionless geometry factor that depends on the geometry of the initial flaws, the loading mode, and the boundary conditions [59]. In principle, the first crack strength σ_{fc} scales with K_m and inversely with $\sqrt{a}$. Potential inconsistency between the measured (Table 5) and the calculated values by the equation of fracture mechanics may be traced to the difference in measured max flaw size and the actual max flaw size. The max flaw size in Table 5 is from 64 cross-sections while the initial crack plane might not be accounted for. The flaw size on the first cracking plane might be larger than the observed one. In addition, the microcracks might be activated by the multiple existing flaws on the

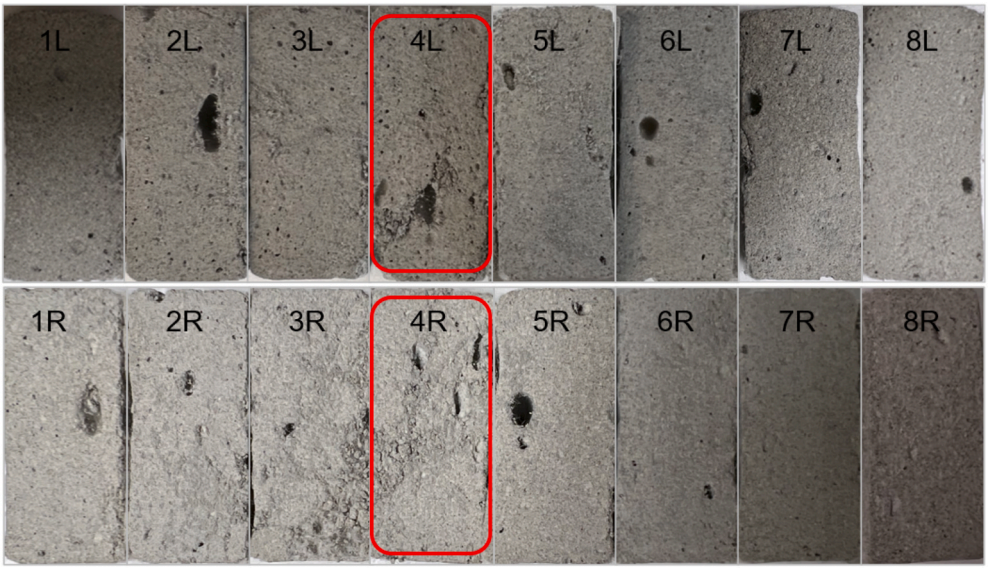

Fig. 11. Cross-section cuts of one specimen of M3-S10.

Table 5
Maximum flaw size, fracture toughness, and first crack strength.

	Max flaw size (mm)	K_m (MPa·m$^{1/2}$)	σ_{fc} (MPa)
M1	4.1 ± 0.6	0.48 ± 0.06	1.56 ± 0.23
M2	3.2 ± 0.9	0.43 ± 0.04	1.61 ± 0.12
M3-S10	5.7 ± 1.1	0.41 ± 0.05	1.51 ± 0.22

*All values are the average for four specimens.

crack plane, resulting in the observed first cracking stress being lower than the calculated values.

As shown in Table 5, M3-S10 had a lower first crack strength (1.51 ± 0.22 MPa) with a lower fracture toughness, and the first crack strength for M2 (1.61 ± 0.12 MPa) was larger than that of M1 (1.56 ± 0.23 MPa) due to the smaller max flaw size. The lower K_m value for M2 and M3-S10 compared with that for M1 is likely associated with the less reactive LC3 binder relative to the OPC binder.

It should be noted that polycarboxylate superplasticizers (PCEs) indeed exhibit the foaming behavior due to the co-surfactant effect caused by the unreacted monomers with surface tension properties during the manufacturing of PCEs [60]. To solve this issue, the unreacted monomers are removed to improve the purity of the co-polymers and the quality of commercial PCEs. Besides, the chemical structures of PCEs also affect their performance in cement-based materials [57]. Related studies show that the air-entraining capability of PCEs is influenced by the type (e.g. functional groups of the chemical structure) and the dosage used in the mixing process [61,62]. The pores in fresh cement mortar caused by PCEs are in the air content range of 2%–6% and the size range of 100–1600 μm, and the large pores (1200–1600 μm) only account for 0.6%–1.6% [61]. Even in aerated concrete where surfactants were used deliberately, the air content caused by large air bubbles (1000–2000 μm) only accounts for 1.65%–3.9% [63]. However, based on the theory of ECC design, the microcracks in ECC are initiated by the large flaws/defects in the crack plane, and the size is always at the millimeter level [64–66], which is also confirmed by the result discussed above. Therefore, the pores caused by PCEs are not the root cause of multiple cracking if large flaws (mm level) exist in ECC. In addition, the matrix fracture toughness and compressive strength (Section 3.3.1) of M3 serial mixtures with different SP dosages have small variations, so the effect caused by the SP dosage used in this study on the matrix performance is negligible. This is consistent with the previous research to find a much smaller impact of chemical admixtures on the matrix mechanical properties [27,56].

Hence, most flaw sizes at the mm level as counted in this section are caused during the mixing process after fiber addition. Except for the hydrophobicity of PP fiber, the mixing process also affects the air entrapment of fresh composite since air bubbles were easily introduced during the mixing process after adding fibers, especially with a longer mixing time and higher mixing speed for better fiber dispersion. The maximum flaw size distribution of M3 series specimens with varying SP content and the corresponding lognormal fit curves are shown in Fig. 12. The entrapped air during mixing accounts for the initial flaws in the composite. Due to the difference in matrix fresh properties, the entrapped air after fiber addition varied. As discussed above, most air voids are caused by fiber addition due to the hydrophobicity of PP fibers, with much less impact of SP content. The matrix fracture toughness for the M3 series is at a similar level (0.40–0.41 MPa m$^{1/2}$). According to linear elastic fracture mechanics, the first crack strength is linearly related to $1/\sqrt{a}$, which roughly follow the data trend in Fig. 13. The low R square of the linear fitting relation in Fig. 13 can be attributed to the difference between the maximum large flaw size in the initial crack plane and the observed cross-sections as discussed above. The maximum

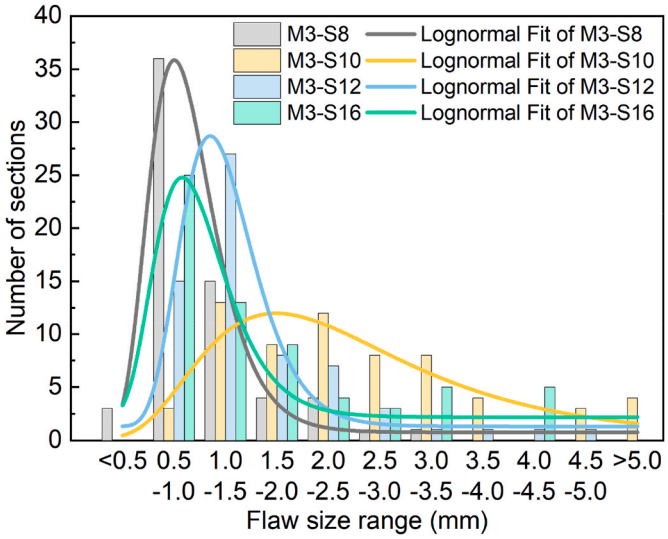

Fig. 12. Maximum flaw size distribution of M3 with different SP content.

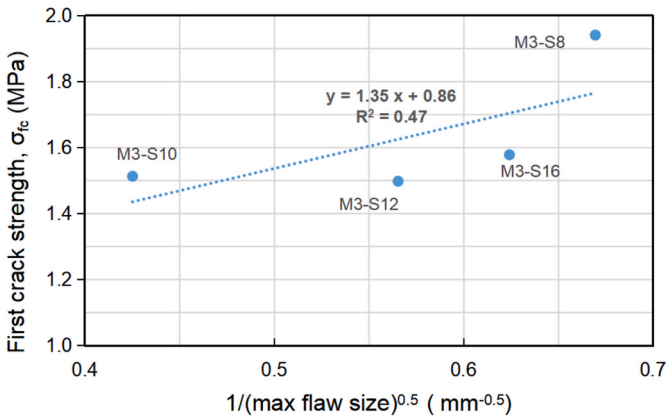

Fig. 13. The relationship between first crack strength and maximum flaw size.

flaw size to initiate the first crack might be larger than the observed value and leads to a relatively low correlation coefficient.

3.2.3. Porosity and density

The porosity for each mixture was calculated based on Eq. (5), using the measured bulk densities ρ_0 and computed particle densities ρ, as shown in Fig. 14. The flaws (air voids) lead to a variety of bulk densities. M3-S10 has the lowest bulk density and highest porosity due to more large-scale flaw size. This can be explained from the viewpoint of air void during the mixing process. As discussed above, although mixing fresh mortar would introduce entrapped air, most air voids are caused by fiber addition due to the change of flowability and the hydrophobicity of PP fibers. Furthermore, a more viscous matrix caused by a low SP content further increased the viscosity after fiber dispersion, which created a stronger shearing effect during fiber mixing and enhanced the fiber dispersion uniformity. Meanwhile, the reduced flowability made the fresh composite hold together and tend to move as a unit with more uniform consistency, which caused less air entrapment, resulting in a lower porosity of the ECC composite. For mortar with high viscosity due to lower SP content (M3-S8), the flowability reduces further with fiber addition, and thus a small volume of air is entrapped during the mixing process. With increased SP content (M3-S10), the flowability can remain in a proper range even after fiber addition. In addition, sufficient mixing with longer mixing time and large mixing speed contributes to air voids entrapping. However, with further increasing SP content (M3-S12, M3-S16), the mortar viscosity is reduced but the flowability of the fresh composite is not enhanced accordingly due to bleeding. Bleeding removes water, resulting in an increase in density and reduction in porosity. Despite the compromised density and high porosity for M3-S10, the first crack was activated at lower stress (Fig. 13). Higher porosity is also beneficial for crack initiation and thus for multiple cracking, which will be discussed in Section 3.3.2.

3.3. Composite properties

The compressive strength, uniaxial tensile stress-strain relation, crack width, and fiber bridging-stress crack-opening relation were measured. These properties were interpreted via the observed microstructure as reported in Section 3.2.

3.3.1. Compressive strength

The 28-day average compressive strength of plain matrix (without fiber) and ECC composites are shown in Fig. 15. Compared to OPC-based matrix (M1), the partial replacement of OPC in LC3 binder (M3-S10) reduced the compressive strength of plain matrix by 31% due to abundant unreacted limestone and calcined clay which serve as inert filling particles. The absence of silica sand in M2 made up for the loss of strength by 20% due to the increase of cement content per volume. The influence of SP content on matrix compressive strength was negligible since most of the air entrapment was caused by fiber addition. In general, fiber addition and excessive mixing time introduced additional air and caused a significant decrease in compressive strength by the extent of 41%–56% for all the mixtures.

The compressive strength correlates well with the porosity and density of the composite (Fig. 14). Since M1, M2, and M3-S10 have similar flowability, their porosity is at a similar level (around 20%) despite the different composition, with a similar reduction (54%–56%) in compressive strength between matrix and composite. A more viscous matrix caused by a low SP content (M3-S8) leads to lower porosity, higher density as well as higher compressive strength. Despite improvement in flowability with higher SP content, no gain in compressive strength was observed. Similar findings on the strength loss by fiber addition (PP and PVA) were reported in the literature [25,34,38]. The slight gain in compressive strength of M3-S12 and M3-S16 is likely a result of bleeding and loss of water from the matrix, and is consistent with a lower porosity when compared with M3-S10.

3.3.2. Uniaxial tensile properties

The tensile properties of specimens prepared with different mixture compositions are shown in Table 6. As shown in Fig. 16, the tensile stress-strain curves show significant differences between the mixtures. Compared to OPC-based ECC (M1), the first crack strength and ultimate tensile strength of LC3-based ECC (M3-S10) were slightly lower. The first crack strength and ultimate tensile strength of M2 are higher than that of M3-S10, which indicates a higher fiber bridging in the M2 composite. The distributed flaws in the composite due to entrapped air are beneficial for microcrack initiation and multiple cracking at a low-stress level, reflected by the many small load drops in the strain-hardening branch of the stress-strain curves. In other words, as microcracks are formed, their small opening contributes to the cumulative

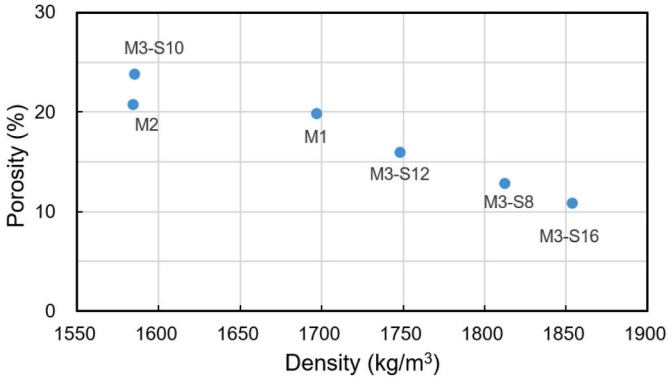

Fig. 14. Relationship between density and porosity.

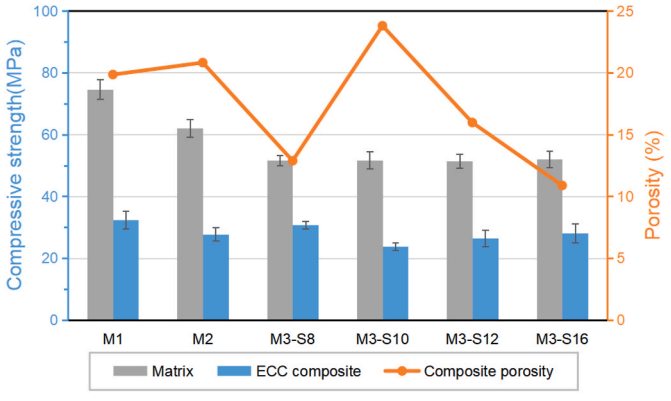

Fig. 15. Relationship between compressive strength and porosity.

Table 6
Tensile properties of specimens at 28 days.

	First crack strength (MPa)	Tensile strength (MPa)	Tensile strain capacity	Crack number	Average crack spacing (mm)
M1	1.56 ± 0.23	2.51 ± 0.09	5.30% ± 0.88%	29 ± 4	2.81 ± 0.49
M2	1.61 ± 0.12	3.01 ± 0.24	8.99% ± 0.28%	78 ± 8	1.04 ± 0.11
M3-S8	1.94 ± 0.16	3.75 ± 0.25	5.35% ± 0.80%	41 ± 12	2.12 ± 0.58
M3-S10	1.51 ± 0.22	2.40 ± 0.13	7.54% ± 1.17%	53 ± 3	1.52 ± 0.09
M3-S12	1.50 ± 0.08	2.62 ± 0.05	5.04% ± 0.42%	47 ± 8	1.75 ± 0.30
M3-S16	1.58 ± 0.40	3.07 ± 0.23	4.06% ± 0.63%	26 ± 9	3.40 ± 1.02

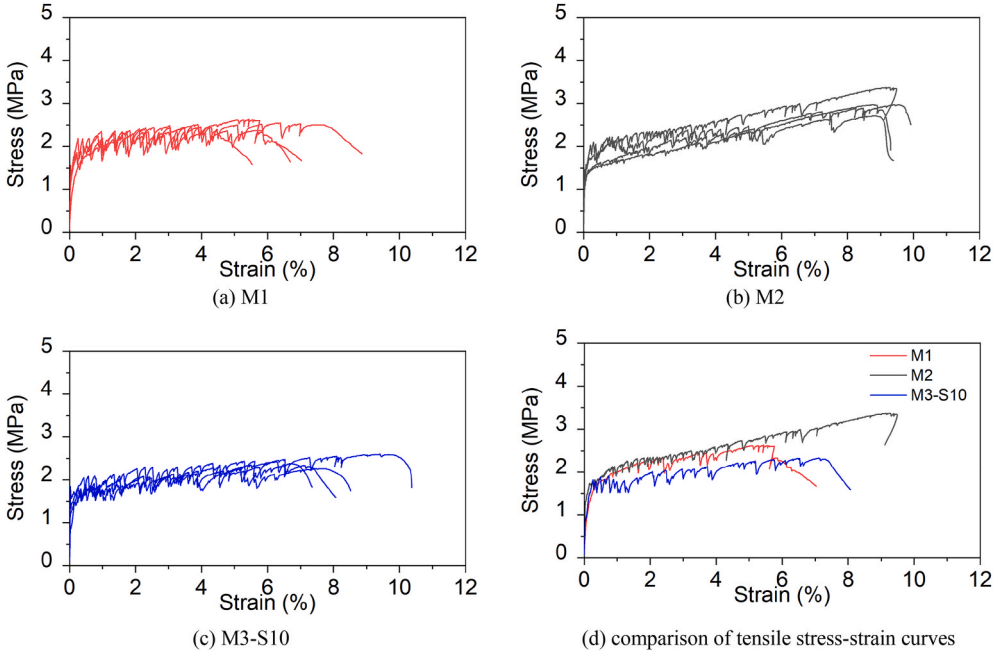

Fig. 16. Tensile stress-strain curves of M1, M2, and M3-S10, showing significant tensile ductility (a) M1 (b) M2 (c) M3-S10 (d) comparison of tensile stress-strain curves.

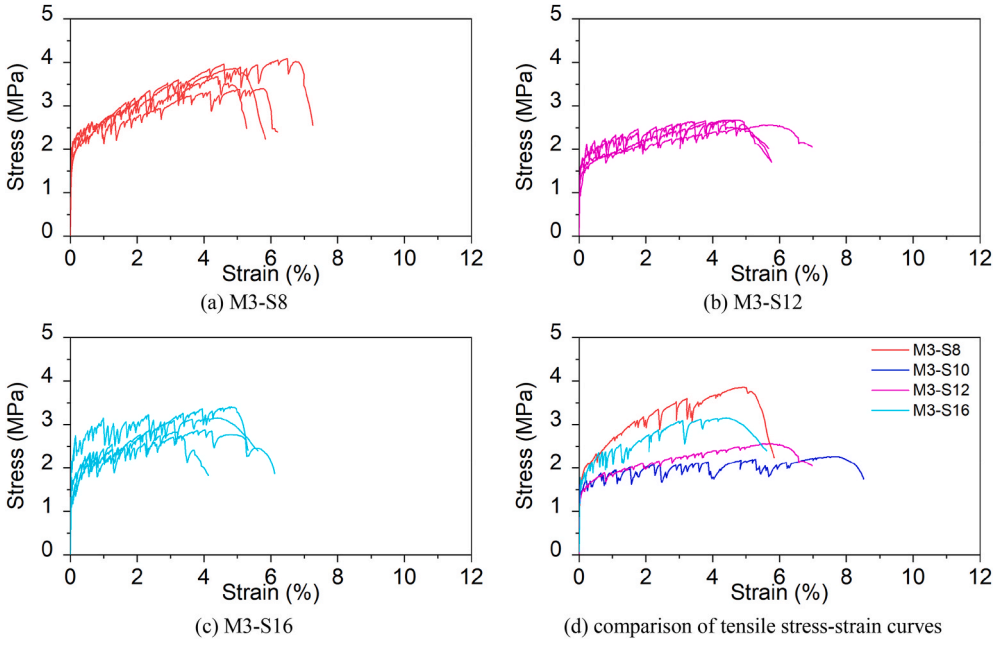

Fig. 17. Tensile stress-strain curves of M3 with different SP content (a) M3-S8 (b) M3-S12 (c) M3-S16 (d) comparison of tensile stress-strain curves.

inelastic deformation of the composite in the strain-hardening stage. All these three mixtures showed saturated multiple cracking behaviors.

The tensile stress-strain curves of M3 with different SP dosages are presented in Fig. 17. Despite identical mixture composition, their tensile behavior differs significantly. With a low amount of superplasticizer (M3-S8), the tensile strength was enhanced compared to M3-S10. This can be explained by the densification of composite. As discussed in Section 3.2.3, the higher viscosity of M3-S8 caused lower porosity and higher density. This densification of the interfacial zone between fiber and matrix led to the increase of interfacial bonding of fiber/matrix, which is beneficial for fiber-bridging capacity. Interfacial bonding refers to frictional bonding since the chemical bonding is negligible due to the hydrophobicity of PP fiber. It is found that there is a relation between composite porosity and tensile strength. Low porosity leads to a high tensile strength due to the enhancement of interfacial bonding and fiber-bridging capacity, but the resulting reduction in crack width also reduces the tensile strain capacity.

The shape of the stress-strain curve can be related to the maximum flaw size distribution in the dogbone specimens. In the M3 series, the slope of the stress-strain curve during strain-hardening (or strain-hardening index) is highest for M3-S8 and lowest (almost flat) for M3-S10. This is consistent with the maximum flaw size distribution curves (Fig. 12) for these mixes. Specifically, M3-S8 has a relatively narrow distribution curve that peaks at a flaw size range 0.5–1.0 mm suggesting that higher tensile stress is necessary to activate these smaller flaws to form the multiple microcracks. In contrast, M3-S10 has a relatively broad distribution curve that peaks at around 1.0–3.5 mm, indicating that more microcracks can be activated by these large flaws with lower stress increasing, and results in a relatively flat slope of the tensile stress-strain curve on the strain-hardening stage, as observed in Fig. 16(c). Similarly, the maximum flaw size distribution curves of M3-S12 and M3-S16 fall between those of M3-S8 and M3-S10 (Fig. 12) while the strain-hardening indices of M3-S12 and M3-S16 also fall between those of M3-S8 and M3-S10 (Fig. 17(d)). This is the first time that the strain-hardening index is consistently correlated to the maximum flaw size distribution in tensile specimens for ECC.

3.3.3. Crack pattern

The evolution of average crack width with tensile strain is presented in Fig. 18. The average crack width was calculated by the gauge length change divided by crack number at each tensile strain of four tension specimens. The average crack width of PP ECC increases at a stable rate during the loading process.

Compared to OPC-based ECC (M1), LC3-based ECC (M3-S10) had a lower first crack strength (Table 6) and activated cracks at a lower strength. The average crack width at 1% tensile strain (80 μm) was close to that of M1 (81.1 μm). However, consistent with the maximum flaw size distribution curves for these two composites (Fig. 10) which show M3-S10 having more large flaws than M1, more cracks were activated with increasing tensile strain at lower tensile stress levels, and thus the average crack width was reduced. The crack width reduction of M3-S10 compared to M1 amounts to 17.8%–22.7% during tensile straining from 2% to 6%.

Compared to M3-S10, M2 showed the tightest crack width among the mixtures (Fig. 18(a)). The average crack width at 2% tensile strain was well controlled at 50.4 μm, and the average crack width was reduced by 29.5%–40.4% in the whole strain-hardening stage. It is likely that the absence of silica sand not only improved the fiber dispersion but also reduced porosity (Fig. 15), which densified the interfacial zone and enhanced the interfacial bonding of fiber and matrix. This is beneficial for a small fiber slippage and a reduction in crack width.

The crack width varies with different SP content in the M3 series (Fig. 18 (b)). M3-S8 shows a tight crack width due to low porosity and the densification of the interfacial zone. However, the crack width increased at a higher rate than that of M3-S12 and exceeded M3-S12 beyond 3% tensile strain. The evolution of crack width was consistent with the tensile stress-strain curve, and the crack opening was increased at large cracking stress according to the relationship between fiber bridging stress (σ)-cracking opening (δ), to be discussed further in the next Section. The crack width of M3-S16 is the highest among these four mixtures since the bleeding of fresh composite caused the change of mixture composition ratio and reduced the water/binder ratio to some extent. The lower w/b ratio densified the matrix and increased the cracking strength as well as the crack width according to the σ-δ relationship.

3.3.4. Fiber bridging stress-crack opening relationship

The measured fiber bridging stress (σ)-cracking opening (δ) relationships from the single-crack test for the various mixes are shown in Fig. 19. Table 7 summarizes the fiber bridging strength. It is noted that the fiber bridging strength is higher than the composite tensile strength. For example, the fiber bridging strength for M1 reached 3.62 MPa, but the tensile strength is only 2.51 MPa (Table 6). This may be anticipated as the composite tensile strength naturally seeks out the weakest specimen cross-section due to nonuniform fiber dispersion. In contrast, the notched cross-section for the single-crack test was pre-determined and did not ensure the weakest cross-section.

The LC3-based ECC (M3-S10) has a lower fiber bridging strength (2.54 MPa) than OPC-based ECC (M1, 3.62 MPa) due to the weaker interfacial bonding caused by the partial replacement of cement in mixture composition. As discussed above, the absence of silica sand in M2 and the lower porosity enhanced the interfacial bonding and thus its fiber bridging capacity (3.41 MPa), and reduced the crack opening.

The SP content caused the variation of microstructure and fiber bridging. M3-S8 with low porosity and M3-S10 with high porosity show the highest and lowest fiber bridging strength, 4.14 MPa and 2.54 MPa, respectively. Relatively low porosity in M3-S12 densified the matrix, resulting in a higher fiber bridging strength compared to M3-S10.

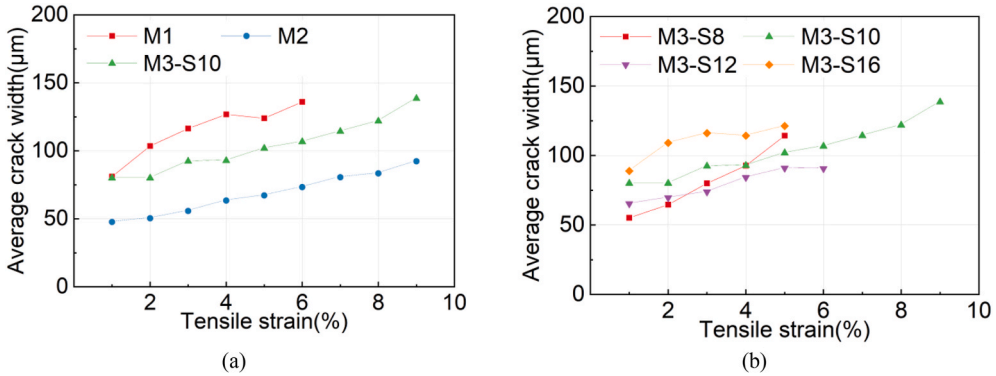

Fig. 18. Evolution of average crack width with tensile strain as influenced (a) by matrix composition, and (b) by SP content.

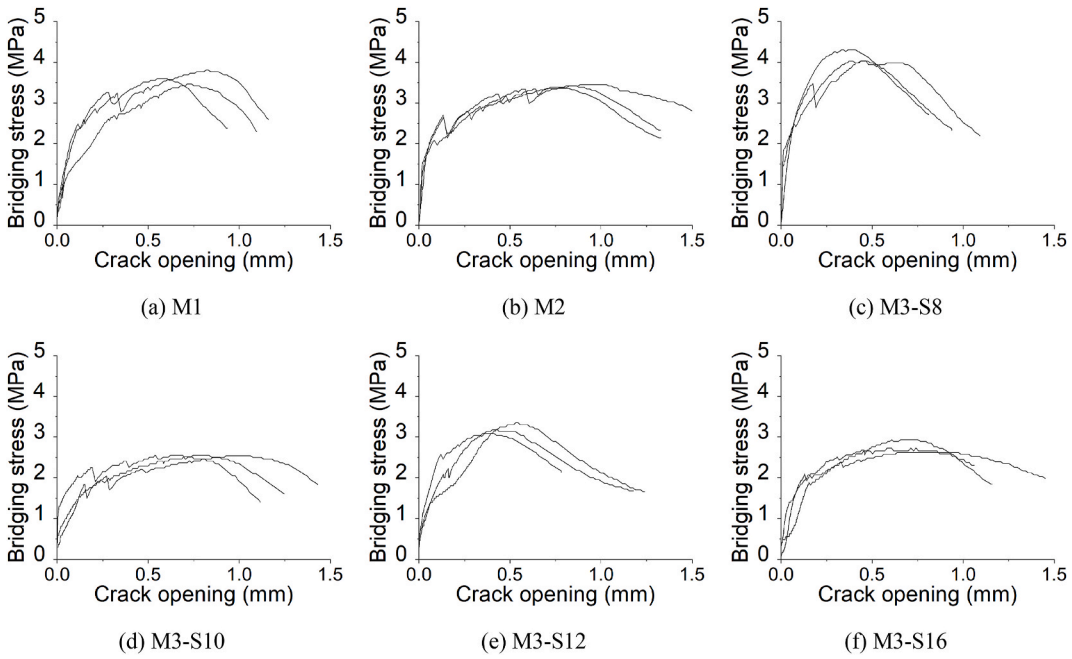

Fig. 19. Fiber bridging stress-crack opening (σ−δ) curves (a) M1 (b) M2 (c) M3-S8 (d) M3-S10 (e) M3-S12 (f) M3-S16.

Table 7
Fiber bridging strength (σ_0) and PSH calculation.

	σ_0 (MPa)	σ_{fc} (MPa)	J_b' (J/m^2)	J_{tip} (J/m^2)	PSH index energy	PSH index strength
M1	3.62	1.56	584.35	11.3	51.7	2.3
M2	3.41	1.61	466.45	10.9	42.8	2.1
M3-S8	4.14	1.94	362.35	11.2	32.4	2.1
M3-S10	2.54	1.51	371.27		33.1	1.7
M3-S12	3.21	1.50	361.22		32.3	2.1
M3-S16	2.76	1.58	376.85		33.6	1.7

However, SP overdosage in M3-S16 not only caused bleeding but relatively poor fiber dispersion. Thus, the fiber bridging capacity was exhausted at a lower strength. Also, the slope of the σ-δ curve is related to the fiber stiffness, modulus, strength, and interfacial bonding between fiber/matrix. M3-S8 shows the highest slope due to the enhancement of interfacial bonding caused by the low porosity. At the early phase of the strain-hardening stage, despite the higher stress than that of M3-S12, the crack opening of M3-S8 is much smaller due to the highest slope according to the σ-δ relationship. However, as discussed in Section 3.3.2, with the narrow flaw size distribution in a small size range, the microcracks need to be activated at higher cracking stress. This also causes a much larger increase in the crack opening even with a relatively high slope of the σ-δ curve, resulting in a higher ultimate crack width of M3-S8 than that of M3-S10 and M3-S12.

A large margin between complementary energy J_b' (defined as the area to the left of σ−δ relation up to peak load) and crack tip toughness J_{tip} ($= K_m^2/E$) as well as between fiber bridging capacity (σ_0) and first crack strength (σ_{fc}) favors robust tensile strain-hardening [67]. The pseudo-strain-hardening (PSH) value has been used to quantify the potential of hardening straining performance as below:

$$PSH\ energy = \frac{J_b'}{J_{tip}} \tag{6}$$

$$PSH\ strength = \frac{\sigma_0}{\sigma_{fc}} \tag{7}$$

These two PSH values should be larger than 1 to ensure strain-hardening performance theoretically. Due to the inhomogeneity in the material, an empirical threshold PSH index was recommended for ensuring robust strain hardening [23,67]. For PP fiber, the recommended PSH value was $PSH_{strength} = 2$, and $PSH_{energy} = 3$, respectively. Yang [23] found that the strength criterion for PP fiber is difficult to achieve compared to the energy criterion, in contrast to PVA fiber. This is also confirmed by the PSH values summarized in Table 7. The PSH index for the energy criterion is far larger than the threshold value, and this is comparable to the previous literature about PP-ECC [25,34] and larger than that of PVA ECC [68]. Although the PSH index for the strength criterion ranges from 1.7 to 2.3, which is close to the threshold value, the specimens show saturated multiple cracking.

4. Conclusions

This study investigates the complex relationships between composition, material processing, microstructure, and composite properties of an ECC with a lower embodied-carbon binder, Limestone Calcined Clay Cement (LC3), and lower-cost PP fiber. The influence of matrix fresh properties, fiber dispersion uniformity, and flaw size distribution on composite mechanical performance was investigated experimentally. The following conclusions can be drawn:

- The change of composition altered the fresh properties. LC3 binder was found to increase the viscosity of the ECC mortar (without fibers). The presence of silica sand and increasing SP content reduce the yield stress and viscosity of mortar paste.
- Modification of matrix viscosity was found to have a direct impact on material microstructures. An increase in matrix viscosity tends to

improve fiber dispersion uniformity and reduce the maximum flaw size as well as porosity.

- The composite macro-mechanical properties of the various mixes can be traced back to the changes in microstructures as impacted by fresh properties. Large maximum flaw size leads to low first crack strength, beneficial for microcrack initiation. Furthermore, increased porosity enhances tensile ductility but compromises the tensile and compressive strength. The fiber bridging capacity of PP-ECC is enhanced by the absence of silica sand, and the low porosity in the LC3-based mixture. This is likely a result of enhanced interfacial bonding associated with a lower porosity in the interfacial transition zone. The enhanced fiber bridging capacity leads to a reduction in crack width in LC3-PP-ECC.

The LC3-PP-ECC studied possesses a compressive strength (20–32 MPa) lower than that of PVA-ECC. However, the tensile ductility (4%–9%) and crack width (50 μm at 2% tension strain) are comparable with traditional PVA ECC. Based on the green credential of LC3-PP-ECC, the promising performance, and the improved understanding of the underlying microstructure and micromechanisms, further studies on LC3-PP-ECC mechanical and durability performance are warranted.

Declaration of competing interest

The authors declare that they have no known competing financial interests or personal relationships that could have appeared to influence the work reported in this paper.

Data availability

Data will be made available on request.

Acknowledgment

This research is financially supported by ARPA-e funding (No. DE-AR0001141) from the US Department of Energy to the University of Michigan. Materials supplied from Boral Resources (fly ash), and BASF (superplasticizer) are gratefully acknowledged.

References

[1] V.C. Li, S. Wang, C. Wu, Tensile strain-hardening behavior or polyvinyl alcohol engineered cementitious composite (PVA-ECC), ACI Mater. J. 98 (2001) 483–492.
[2] H. Ma, C. Yi, C. Wu, Review and outlook on durability of engineered cementitious composite (ECC), Construct. Build. Mater. 287 (2021).
[3] H. Liu, Q. Zhang, V. Li, H. Su, C. Gu, Durability study on engineered cementitious composites (ECC) under sulfate and chloride environment, Construct. Build. Mater. 133 (2017) 171–181.
[4] M. Şahmaran, V.C. Li, Durability of mechanically loaded engineered cementitious composites under highly alkaline environments, Cem. Concr. Compos. 30 (2008) 72–81.
[5] M. Şahmaran, V.C. Li, Durability properties of micro-cracked ECC containing high volumes fly ash, Cement Concr. Res. 39 (2009) 1033–1043.
[6] D. Shoji, Z. He, D. Zhang, V.C. Li, The greening of engineered cementitious composites (ECC): a review, Construct. Build. Mater. 327 (2022) 1–19.
[7] H. Ritchie, M. Roser, CO_2 and greenhouse gas emissions, Our World Data (2020). https://ourworldindata.org/emissions-by-fuel#per-capita-how-do-coal-oil-gas-and-cement-emissions-compare.
[8] A. Mokhtar, M. Nasooti, A decision support tool for cement industry to select energy efficiency measures, Energy Strategy Rev. 28 (2020), 100458.
[9] Y.K. Verma, B. Mazumdar, P. Ghosh, Thermal energy consumption and its conservation for a cement production unit, Environ. Eng. Res. 26 (2021) 1–9.
[10] J.S.J. van Deventer, C.E. White, R.J. Myers, A Roadmap for Production of Cement and Concrete with Low-CO2 Emissions, Springer Netherlands, 2021.
[11] M. Schneider, The cement industry on the way to a low-carbon future, Cement Concr. Res. 124 (2019), 105792.
[12] K. Scrivener, F. Martirena, S. Bishnoi, S. Maity, Calcined clay limestone cements (LC3), Cement Concr. Res. 114 (2018) 49–56.
[13] S. Bishnoi, S. Maity, A. Mallik, S. Joseph, S. Krishnan, Pilot scale manufacture of limestone calcined clay cement : the Indian experience, Indian Concr. J. 88 (2014) 22–28.
[14] R.T. Rios, F. Lolli, L. Xie, Y. Xie, K.E. Kurtis, Cement and Concrete Research Screening candidate supplementary cementitious materials under standard and accelerated curing through time-series surface resistivity measurements and change-point detection, Cement Concr. Res. 148 (2021), 106538.
[15] R. Gettu, A. Patel, V. Rathi, S. Prakasan, A.S. Basavaraj, S. Palaniappan, S. Maity, Influence of supplementary cementitious materials on the sustainability parameters of cements and concretes in the Indian context, Mater. Struct. Constr. 52 (2019) 1–11.
[16] M. Antoni, J. Rossen, F. Martirena, K. Scrivener, Cement substitution by a combination of metakaolin and limestone, Cement Concr. Res. 42 (2012) 1579–1589.
[17] S. Sánchez Berriel, A. Favier, E. Rosa Domínguez, I.R. Sánchez MacHado, U. Heierli, K. Scrivener, F. Martirena Hernández, G. Habert, Assessing the environmental and economic potential of limestone calcined clay cement in Cuba, J. Clean. Prod. 124 (2016) 361–369.
[18] D. Zhang, B. Jaworska, H. Zhu, K. Dahlquist, V.C. Li, Engineered Cementitious Composites (ECC) with limestone calcined clay cement (LC3), Cem. Concr. Compos. 114 (2020), 103766.
[19] J. Yu, H.-L.L. Wu, C.K.Y. Leung, Feasibility of using ultrahigh-volume limestone-calcined clay blend to develop sustainable medium-strength Engineered Cementitious Composites (ECC), J. Clean. Prod. 262 (2020), 121343.
[20] H. Zhu, D. Zhang, T. Wang, H. Wu, V.C. Li, Mechanical and self-healing behavior of low carbon engineered cementitious composites reinforced with PP-fibers, Construct. Build. Mater. 259 (2020), 119805.
[21] H. Zhu, K. Yu, V.C. Li, Sprayable engineered cementitious composites (ECC) using calcined clay limestone cement (LC3) and PP fiber, Cem. Concr. Compos. 115 (2021), 103868.
[22] L. Wang, N. Ur, I. Curosu, Z. Zhu, M. Abdul, B. Beigh, M. Liebscher, L. Chen, D.C. W. Tsang, S. Hempel, V. Mechtcherine, Cement and Concrete Research on the use of limestone calcined clay cement (LC 3) in high-strength strain-hardening cement-based composites (HS-SHCC), C 144 (2021) 1–13.
[23] E.H. Yang, V.C. Li, Strain-hardening fiber cement optimization and component tailoring by means of a micromechanical model, Construct. Build. Mater. 24 (2010) 130–139.
[24] Q. Jin, V.C. Li, Development of lightweight engineered cementitious composite for durability enhancement of tall concrete wind towers, Cem. Concr. Compos. 96 (2019) 87–94.
[25] B. Felekoglu, K. Tosun-Felekoglu, R. Ranade, Q. Zhang, V.C. Li, Influence of matrix flowability, fiber mixing procedure, and curing conditions on the mechanical performance of HTPP-ECC, Compos. B Eng. 60 (2014) 359–370.
[26] K. Tosun-Felekoğlu, E. Gödek, M. Keskinateş, B. Felekoğlu, Utilization and selection of proper fly ash in cost effective green HTPP-ECC design, J. Clean. Prod. 149 (2017) 557–568.
[27] E. Yang, M. Sahmaran, Y. Yang, V.C. Li, Rheological Control in Production of Engineered Cementitious Composites, 2009, pp. 357–366.
[28] M. Li, V.C. Li, Rheology, fiber dispersion, and robust properties of engineered cementitious composites, Mater. Struct. Constr. 46 (2013) 405–420.
[29] R. Ranade, M.D. Stults, B. Lee, V.C. Li, Effects of fiber dispersion and flaw size distribution on the composite properties of PVA-ECC, RILEM Bookseries 2 (2012) 107–114.
[30] M. Cao, W. Si, C. Xie, Relationship of rheology, fiber dispersion, and strengths of polyvinyl alcohol fiber-reinforced cementitious composites, ACI Mater. J. 117 (2020) 191–204.
[31] W. Si, M. Cao, L. Li, Establishment of fiber factor for rheological and mechanical performance of polyvinyl alcohol (PVA) fiber reinforced mortar, Construct. Build. Mater. 265 (2020).
[32] H.L. Wu, J. Yu, D. Zhang, J.X. Zheng, V.C. Li, Effect of morphological parameters of natural sand on mechanical properties of engineered cementitious composites, Cem. Concr. Compos. 100 (2019) 108–119.
[33] B. Felekoğlu, K. Tosun-Felekoğlu, E. Gödek, A novel method for the determination of polymeric micro-fiber distribution of cementitious composites exhibiting multiple cracking behavior under tensile loading, Construct. Build. Mater. 86 (2015) 85–94.
[34] M. Keskinateş, B. Felekoğlu, The influence of mineral additive type and water/binder ratio on matrix phase rheology and multiple cracking potential of HTPP-ECC, Construct. Build. Mater. 173 (2018) 508–519.
[35] D. Zhang, H. Zhu, M.M. Hou, K.E. Kurtis, P.J.M. Monteiro, V.C. Li, Optimization of matrix viscosity improves polypropylene fiber dispersion and properties of engineered cementitious composites, Construct. Build. Mater. 346 (2022), 128459.
[36] M. Li, J. Han, Y. Zhou, P. Yan, A rheological model for evaluating the behavior of shear thickening of highly Flowable mortar, Molecules 26 (2021).
[37] J. Zhou, S. Qian, G. Ye, O. Copuroglu, K. Van Breugel, V.C. Li, Improved fiber distribution and mechanical properties of engineered cementitious composites by adjusting the mixing sequence, Cem. Concr. Compos. 34 (2012) 342–348.
[38] K. Tosun-Felekoğlu, B. Felekoğlu, R. Ranade, B.Y. Lee, V.C. Li, The role of flaw size and fiber distribution on tensile ductility of PVA-ECC, Compos. B Eng. 56 (2014) 536–545.
[39] A. Anil Thakare, S. Siddique, S.N. Sarode, R. Deewan, V. Gupta, S. Gupta, S. Chaudhary, A study on rheological properties of rubber fiber dosed self-compacting mortar, Construct. Build. Mater. 262 (2020), 120745.
[40] K. Vance, G. Sant, N. Neithalath, The rheology of cementitious suspensions: a closer look at experimental parameters and property determination using common rheological models, Cem. Concr. Compos. 59 (2015) 38–48.
[41] A. Kostrzanowska-Siedlarz, J. Gołaszewski, Rheological properties and the air content in fresh concrete for self compacting high performance concrete, Construct. Build. Mater. 94 (2015) 555–564.
[42] D.P. Bentz, C.F. Ferraris, M.A. Galler, A.S. Hansen, J.M. Guynn, Influence of particle size distributions on yield stress and viscosity of cement-fly ash pastes, Cement Concr. Res. 42 (2012) 404–409.

[43] ASTM, Standard Test Method for Flow of Hydraulic Cement Mortar, 2007, p. C1437.
[44] JSCE, Recommendations for Design and Construction of High Performance Fiber Reinforced Cement Composites with Multiple Fine Cracks, Japan Soc. Civ. Eng., 2008.
[45] ASTM C109, ASTM C109/C109M - 20b, Standard test method for compressive strength of hydraulic cement mortars (using 2-in. Or [50 mm] cube specimens), Annu. Book ASTM Stand. (2016) 9, 04.
[46] ASCE, Standard Test Method for Linear-Elastic Plane-Strain Fracture Toughness KIc of Metallic Materials, E399, 2019, pp. 1–35.
[47] V.C. Li, D.K. Mishra, H.C. Wu, Matrix design for pseudo-strain-hardening fibre reinforced cementitious composites, Mater. Struct. 28 (1995) 586–595.
[48] B.Y. Lee, J.K. Kim, J.S. Kim, Y.Y. Kim, Quantitative evaluation technique of Polyvinyl Alcohol (PVA) fiber dispersion in engineered cementitious composites, Cem. Concr. Compos. 31 (2009) 408–417.
[49] S. Torigoe, T. Horikoshi, A. Ogawa, T. Saito, T. Hamada, Study on evaluation method for PVA fiber distribution in engineered cementitious composite, J. Adv. Concr. Technol. 1 (2003) 265–268.
[50] B.Y. Lee, T. Kim, Y.Y. Kim, Fluorescence characteristic analysis for discriminating fibers in cementitious composites, J. Adv. Concr. Technol. 8 (2010) 337–344.
[51] N. Nair, K. Mohammed Haneefa, M. Santhanam, R. Gettu, A study on fresh properties of limestone calcined clay blended cementitious systems, Construct. Build. Mater. 254 (2020), 119326.
[52] T.R. Muzenda, P. Hou, S. Kawashima, T. Sui, X. Cheng, The role of limestone and calcined clay on the rheological properties of LC3, Cem. Concr. Compos. 107 (2020), 103516.
[53] F. Cassagnabère, P. Diederich, M. Mouret, G. Escadeillas, M. Lachemi, Impact of metakaolin characteristics on the rheological properties of mortar in the fresh state, Cem. Concr. Compos. 37 (2013) 95–107.
[54] R. Li, L. Lei, T. Sui, J. Plank, Effectiveness of PCE superplasticizers in calcined clay blended cements, Cement Concr. Res. 141 (2021), 106334.
[55] L. Lei, M. Palacios, J. Plank, A.A. Jeknavorian, Interaction between polycarboxylate superplasticizers and non-calcined clays and calcined clays: a review, Cement Concr. Res. 154 (2022), 106717.
[56] Z. Tang, C. Litina, A. Al-Tabbaa, Optimisation of rheological parameters and mechanical properties of Engineered Cementitious Composites (ECC) using regression-based models, Construct. Build. Mater. 310 (2021), 125281.
[57] S. Sha, M. Wang, C. Shi, Y. Xiao, Influence of the structures of polycarboxylate superplasticizer on its performance in cement-based materials-A review, Construct. Build. Mater. 233 (2020), 117257.
[58] R. Ranade, V.C. Li, M.D. Stults, T.S. Rushing, J. Roth, W.F. Heard, Micromechanics of high-strength, high-ductility concrete, ACI Mater. J. 110 (2013) 375.
[59] Ted L. Anderson, Fracture Mechanics : Fundamentals and Applications, CRC Press, 2017.
[60] A. Lange, J. Plank, Study on the foaming behaviour of allyl ether-based polycarboxylate superplasticizers, Cement Concr. Res. 42 (2012) 484–489.
[61] Y. He, X. Zhang, W. Hong, L. Shui, X. Wang, H. Wang, L. Peng, Effects of polycarboxylate superplasticisers with various functional groups on the pore structure of cement mortar, Adv. Cement Res. 32 (2020) 510–518.
[62] V. Han, S. Ros, H. Shima, Effects of sand content, superplasticizer dosage, and mixing time on compressive strength of mortar, ACI Mater. J. 110 (2013).
[63] T. Guo, M. Qiao, X. Shu, L. Dong, G. Shan, X. Liu, Y. Guo, Q. Ran, Characteristic analysis of air bubbles on the rheological properties of cement mortar, Construct. Build. Mater. 316 (2022), 125812.
[64] V.C. Li, Tailoring ECC for special attributes: a review, Int. J. Concr. Struct. Mater. 6 (2012) 135–144.
[65] V.C. Li, Engineered Cementitious Composites (ECC): Bendable Concrete for Sustainable and Resilient Infrastructure, Springer Berlin Heidelberg, 2019.
[66] S. Wang, V.C. Li, Tailoring of Pre-existing Flaws in ECC Matrix for Saturated Strain Hardening, Framcos2004, 2004, pp. 1005–1012.
[67] T. Kanda, Design of Engineered Cementitious Composites for Ductile Seismic Resistant Elements, University of Michigan, 1998.
[68] H. Ma, S. Qian, Z. Zhang, Z. Lin, V.C. Li, Tailoring engineered cementitious composites with local ingredients, Construct. Build. Mater. 101 (2015) 584–595.